Journal of Power Sources 221 (2013) 217–227

Contents lists available at SciVerse ScienceDirect

Journal of Power Sources

journal homepage: www.elsevier.com/locate/jpowsour

Novel composite solid state electrolytes on the base of $BaCeO_3$ and CeO_2 for intermediate temperature electrochemical devices

D. Medvedev [a], V. Maragou [b], E. Pikalova [a], A. Demin [a,**], P. Tsiakaras [b,*]

[a] Institute of High Temperature Electrochemistry, Laboratory of Solid Oxide Fuel Cells, 22 S. Kovalevskoy, 620990 Yekaterinburg, Russia
[b] Department of Mechanical Engineering, School of Engineering, University of Thessaly, Pedion Areos, 383 34 Volos, Greece

HIGHLIGHTS

- Novel two-phase SDC–BCS composite materials were prepared by solution combustion synthesis.
- The effect of perovskite content and fuel type on the morphology was investigated.
- Co-presence of perovskite and fluorite phases is favorable due to: (a) thermodynamic stability against CO_2 and (b) low electron contribution to the total conductivity.

ARTICLE INFO

Article history:
Received 5 June 2012
Received in revised form
27 July 2012
Accepted 31 July 2012
Available online 9 August 2012

Keywords:
Mixed ion conductor
Composite electrolyte
Doped ceria
Doped barium cerate
IT-SOFCs
Combustion synthesis

ABSTRACT

In the present work, nano-sized powders of $(1-x)Ce_{0.8}Sm_{0.2}O_{2-\delta}$–$xBaCe_{0.8}Sm_{0.2}O_{3-\delta}$ ($x = 0$, 0.3, 0.5, 0.7 and 1) were obtained by solution combustion synthesis (self-combustion synthesis, SCS) method of nitrate and various types of organic fuels (glycine, glycerin, citric acid and a mixture of citric acid and ethylene glycol). The research results indicate that the finest powders by using the SCS process are formed when the perovskite concentration is decreased in the system under study, as well as when as the fuel glycerin or a mixture of citric acid and ethylene glycol are used. The use of the specific method allows the preparation of dense composite ceramics at 1500 °C. The investigation of the electrical properties of the composites at a wide range of temperatures and oxygen partial pressures shows that $0.5Ce_{0.8}Sm_{0.2}O_{2-\delta}$–$0.5BaCe_{0.8}Sm_{0.2}O_{3-\delta}$ material is characterized by relatively good stability against CO_2, acceptable value of total conductivity and the lowest contribution of electron conductivity in both oxidizing and reducing atmospheres.

1. Introduction

It is widely known that solid oxide fuel cells (SOFCs) are electrochemical devices that convert directly the chemical energy of a fuel into electricity. SOFCs have a great advantage over other energy production systems due to their autonomy, high efficiency, fuel diversity, including among others the possibility to use natural gas and biogas, and their environmental safety [1,2]. Significant efforts have been made to develop commercially profitable generators on the base of SOFCs with low cost and long-term stability. This problem can be partly solved by decreasing the operation temperature to the intermediate temperature (IT) range of 400–750 °C, since the latter enables the use less expensive electrode and interconnector's materials and suppresses stack degradation [3–7].

In turn, the electrolytes for IT-SOFCs have to satisfy specific criteria for effective operation at decreased temperatures: high ionic conductivity and ionic transport number in a wide range of oxygen partial pressures, chemical and physical stability at the operating conditions, accessibility and low cost of raw materials and easy mass production. For the time being, oxygen-ion conductors are mainly used as electrolytes of SOFCs; however, proton-conducting oxides are also an important class for this kind of applications. Despite the fact that considerable research activity has been devoted towards the selection of novel oxide ion and proton conductors as alternative electrolytes to the widely used stabilized zirconia, doped ceria and doped barium cerate oxides

* Corresponding author. Tel.: +30 24210 74065; fax: +30 24210 74050.
** Corresponding author. Tel.: +7 343 3745431; fax: +7 343 3745992.
E-mail addresses: A.Demin@ihte.uran.ru (A. Demin), tsiak@mie.uth.gr (P. Tsiakaras).

0378-7753/$ – see front matter © 2012 Elsevier B.V. All rights reserved.
http://dx.doi.org/10.1016/j.jpowsour.2012.07.120

still remain the most promising materials as electrolytes in the intermediate temperature regime, due to their high ionic conductivity and relatively low cost in comparison with the solid electrolytes based on gallium and scandium oxides [8–17].

In the case of $BaCeO_3$ based materials in addition to oxygen-ion conductivity, in wet hydrogen atmosphere high levels of proton conductivity appear. As a result, the efficiency of a SOFC system with such kind of co-ionic electrolytes is evidently higher than that of a SOFC system based on oxygen-ion conductors. In the work of Demin et al. it was found that the maximum achievable efficiency of a hydrogen-fed SOFC based on the co-ionic electrolyte with proton's transferring number $t_H = 0.5$ is 78 % at 627 °C [18]. According to a thermodynamic analysis, in a methane fed SOFC(H^+) system the fuel utilization reaches 96.5% at the same temperature when the H_2O/CH_4 mole ratio in the feeding fuel mixture corresponds to 2.6 [19]. Therefore, the research for solid oxides with high proton conductivity that are characterized at the same time by stability in carbon dioxide containing atmospheres, seems to be a very important task in view of fabrication of highly efficient electrochemical generators.

Doped $BaCeO_3$ has exhibited poor stability in CO_2, H_2O and other trace spaces (SO_2, SO_3, and H_2S). The partial substitution of Ce by Zr can reduce the tendency of decomposition in CO_2 at high temperatures; however, it results in the decrease of ionic conductivity [20–23]. The stability of solid electrolytes on the base of CeO_2 in vapor and carbon dioxide presence, their catalytic activity towards direct CH_4 oxidation and their chemical compatibility with perovskite cathode materials have been investigated by many authors [24–27]. However di- or trivalent element-doped ceria systems are known to exhibit electronic conduction at high temperatures and low partial pressures of oxygen (pO_2) at the anode side of SOFCs, because of the partial reduction of Ce^{4+} to Ce^{3+}. In turn, the reduction of ceria results in the decrease of the Open Circuit Voltage (OCV) of the cell and consequently in the reduction of the cell's efficiency [28]. Some attempts have been made to suppress the electronic conductivity of ceria-based electrolytes by means of thin barrier layer of yttria-stabilized zirconia [29,30] and rare-earth-doped barium cerate [31, 32] on the anode side. The structural modification of ceria-based solid solutions by co-doping with rare-earth elements or alkali, alkali-earth elements with big effective ionic radius (Cs^{+1}, Sr^{2+}, and Ba^{2+}) leads to an increase of the total oxygen-ionic conductivity in air atmosphere and to the expansion of the electrolytic area due to the partial suppression of ceria's reduction [33,34]. Because of the low solubility of alkali-earth elements in fluorite structure (Ba^{2+} – 2 mol.%, Sr^{2+} – 8 mol.%) the spectrum of such modified materials with enhanced electrolytic properties is narrow [35]. The advantage of composite ceramics consists of the ability to produce a wide range of materials with different functional properties, including electrolyte materials. $BaCeO_3$ and CeO_2-based solid solutions are perspective materials for composites due to their chemical compatibility and similar values of thermal expansion coefficient (TEC) [36–39].

In terms of statistically distributed phases of fluorite (the structure of cerium oxide) and perovskite (barium cerate structure) over the volume of the composites, the stability of such materials in CO_2 and H_2O can be significantly increased. In addition, the electrolytic area of the composite electrolytes is expected to be wider because of the decrease of the electronic conductivity at low pO_2 by blocking with barium cerate phase, and vice versa, the reduction of the hole conductivity in oxidizing conditions caused by the blocking with ceria phase. Recent investigations showed that as a rule, the total conductivity of composites slightly decreases with the increase of cerate content in the temperature range of 600–900 °C. However, at lower temperatures the reverse tendency takes place because of the decrease of activation energy [40]. Despite the decrease of conductivity, the power density of the composite electrolyte-based SOFCs raises in comparison with ceria-based ones [41–43], probably due to the lower values of electronic conductivity in reducing atmospheres, which in turn leads to the increase of OCV. It was found that the OCV value of an electrochemical cell with $BaCe_{0.8}Sm_{0.2}O_{3-\delta}$–$Ce_{0.8}Sm_{0.2}O_{2-\delta}$ (1:1 weight relation) is higher by 250 mV than in the case of $Ce_{0.8}Sm_{0.2}O_{2-\delta}$ [42,44].

However, the total conductivity data of $BaCeO_3$–CeO_2 composites, presented in literature, were investigated in air, and there is a lack of information concerning possible deterioration of the electronic conductivity. Furthermore, it would be interesting to investigate the influence of the preparation method of the composites on their sintering behavior, as well as on their structural and electrical properties. In the present work, the influence of both the content of the cerate phase and the kind of the organic fuel on the key properties of composites $(1-x)Ce_{0.8}Sm_{0.2}O_{2-\delta}$–$xBaCe_{0.8}Sm_{0.2}O_{3-\delta}$ ($x = 0$; 0.3; 0.5; 0.7; 1) produced by combustion synthesis method, widely used for the preparation of complex chemical compositions [45–48] is investigated. As a rule, in order to prepare composites, the basic components are synthesized separately with following mixing. To our knowledge, only two published articles about the one-step citric acid–nitrate gel combustion method were found [41,49]. In the present work, the mixing of the calculated quantities of all components was also performed before combustion for more uniform elements' distribution in the composite matrix. The optimal conditions of powder calcinations and gastight ceramics' preparation were determined according to the thermogravimetric (TG) and thermochemical (DSC) analyses and dilatometric measurements. The investigation of the dependence of the total conductivity on the oxygen partial pressure in the range of 10^{-20}–0.21 atm is presented.

2. Experimental

$Ba(NO_3)_2$ (purity 99.95%), $Ce(NO_3)_3 \cdot 6H_2O$ (purity 99.9%) and $Sm(NO_3)_3 \cdot 6H_2O$ (purity 99.9%) were used as starting materials. The compositions of $xBaCe_{0.8}Sm_{0.2}O_{3-\delta}$–$(1-x)Ce_{0.8}Sm_{0.2}O_{2-\delta}$ ($x = 0$, 0.3, 0.5, 0.7 and 1) were obtained by employing the solution combustion synthesis method (self-combustion synthesis, SCS) of the corresponding nitrates and glycine, glycerin, citric acid and mixture of citric acid and ethyleneglycol (mol fraction 1:5) as the fuel. The technological features of this method are described in the work of Chen et al. [50]. The designations of oxide powders are listed in Table 1.

The necessary amounts of nitrates and fuel were calculated according to the reaction that takes place in the SCS. For the preparation of the oxide powders by Pechini method, the corresponding nitrates were chosen in a stoichiometric ratio with citric acid. The TG and DSC studies of the powders obtained by the SCS method were carried out on synchronous thermal analyzer STA 449C Jupiter® manufactured by NETZSCH (Germany) in air atmosphere, at temperatures of 20–1500 °C. In order to remove the undecomposed organic particles and nitrates and to obtain the

Table 1
Compositions for the present study.

Compositions	Designation	Fuel
$Ce_{0.8}Sm_{0.2}O_{2-\delta}$	SDC-3	Glycerin
$0.7Ce_{0.8}Sm_{0.2}O_{2-\delta}$–$0.3BaCe_{0.8}Sm_{0.2}O_{3-\delta}$	7SDC–3BCS-1	Glycine
	7SDC–3BCS-2	Citric acid
	7SDC–3BCS-3	Glycerin
	7SDC–3BCS-4	Citric acid + ethyleneglycol
$0.5Ce_{0.8}Sm_{0.2}O_{2-\delta}$–$0.5BaCe_{0.8}Sm_{0.2}O_{3-\delta}$	5SDC–5BCS-3	Glycerin
$0.3Ce_{0.8}Sm_{0.2}O_{2-\delta}$–$0.7BaCe_{0.8}Sm_{0.2}O_{3-\delta}$	3SDC–7BCS-3	Glycerin
$BaCe_{0.8}Sm_{0.2}O_{3-\delta}$	BCS-3	Glycerin

corresponding oxide components, the powders after SCS were annealed at 600 °C for 5 h, and then calcined at 1100 °C for 3 h.

The obtained powders were examined by X-ray powder diffraction analysis (XRD, DMAX-2500 RIGAKU). The scans ranged between $20^\circ \le 2\theta \le 80^\circ$ with an interval of $0.5^\circ\ min^{-1}$. The identification of the materials' phase composition, crystal structure and particle size were performed according to JCPDS data file by employing MDI Jade 6 software. The apparent crystallite size was calculated using the Scherrer's equation as follows:

$$D_{hkl} = \frac{0.9\lambda}{\beta \cos\theta}, \quad (1)$$

where λ is the wavelength, β the full-width-half-maximum of the peak and θ the Bragg's angle of {*hkl*} reflection.

The specific surface area of the powders was measured by Brunauer–Emmett–Teller (BET) analysis. The particle size of the calcined powders was calculated according to the following equation:

$$D_{BET} = \frac{6 \times 10^3}{\rho_{th} S_{BET}}, \quad (2)$$

where S_{BET} is the specific surface area and ρ_{th} the material's theoretical density ($\sim 7.2\ g\ cm^{-3}$ for SDC, $\sim 6.3\ g\ cm^{-3}$ for BCS). The theoretical density of the composite materials was calculated as a partial sum of the theoretical density of each phase.

The morphology of the powders and the surface of the sintered samples were investigated by scanning electron microscopy (SEM, JSM-5900 LV). The calcined powders were milled at a planetary mill (Fritsch Pulverisette 6) for 1 h with a rate of rotation equal to $350\ min^{-1}$. The powder materials were compacted by magnetic impulsing pressing [51]. The investigation of the kinetics for pressing samples during sintering was carried out by dilatometer equipment (DIL 402C/3/G, NETZSCH). The sintering regime of the ceramic samples was chosen according to the data of the dilatometric measurements.

The values of the total conductivity of the samples were measured by four-probe DC method in the interval of 500–900 °C (in wet air atmosphere) and in a wide oxygen partial pressure range (10^{-20}–0.21 atm) at 750 and 900 °C.

3. Results and discussion

SCS process can be represented as follows:

$$x\mathrm{Ba(NO_3)_2} + 0.8\mathrm{Ce(NO_3)_3 \cdot 6H_2O} + 0.2\mathrm{Sm(NO_3)_3 \cdot 6H_2O} + \varphi \mathrm{C_aH_bN_cO_d} \rightarrow \mathrm{Ba_xCe_{0.8}Sm_{0.2}O_{1.9+x}} + a\varphi\mathrm{CO_2} + (6 + 1/2b\varphi)\mathrm{H_2O} + (2x + 3 + \varphi c)/2\mathrm{N_2}, \quad (3)$$

where φ is a stoichiometric amount of the fuel determined by the equation of the redox reaction between organic compounds ($C_aH_bN_cO_d$), Ce^{3+} ions and nitrate groups, whereas *a*, *b*, *c* and *d* are the numbers of atoms of C, H, N and O in the fuel, respectively. The parameter φ can be determined by the equation that relates the oxygen balance in the left and in the right side of the reaction (3):

$$\varphi = \frac{5x + 7.1}{2a + b/2 - d}. \quad (4)$$

In Fig. 1 it can be observed that the powders of $(1-x)\mathrm{Ce_{0.8}Sm_{0.2}O_{2-\delta}}$–$x\mathrm{BaCe_{0.8}Sm_{0.2}O_{3-\delta}}$ obtained with different types of fuels present highly porous structure, apparently due to the large amount of gases evolved during the SCS (reaction (3)). For example, the synthesis of cerium oxide using ethylene glycol as the fuel by SCS for 1 mol of cerium nitrate source is formed about 12.5 mol of gases [50]. A similar situation is observed in the synthesis of barium cerate with glycine by SCS: for 1 mol $\mathrm{BaCe_{0.8}Y_{0.2}O_{3-\delta}}$ formed about 16 mol of gases [52].

The morphology and the crystallite size of the powders depend on the type of the organic agent. The corresponding results for the examined materials are presented in Fig. 2. It is known that important factors in goal-directed synthesis of submicron and nanoscale oxide materials by SCS are the enthalpy and the adiabatic temperature of the redox reaction. In this case there is a tendency to reduce the particle size when the reaction enthalpy and the adiabatic temperature are reduced.

The decrease of these parameters can be achieved, for example, by replacing organic fuels containing NH_2- on HO- or HOOC-functional groups [50,53,54]. In addition, it is necessary to take into account the complexion and polymerization properties of organic materials used as fuel in the SCS process [48,55]. Using glycerin and a mixture of citric acid and ethylene glycol leads to intense foaming organometallic complex before SCS and the subsequent formation of fine oxide powder (Fig. 2c and d), whereas the use of glycine and citric acid leads to the rapid combustion of fuel/nitrates mixture and the formation of partially sintered (agglomerated) powder (Fig. 2a).

For further investigations we chose glycerin as a fuel and investigated the features of powders base individual phase and composite materials. Fig. 3 shows the TG-DSC curves for SDC-3, BCS-3 and 7SDC–3BCS-3 powders. For SDC-3 sample, the powder mass in the temperature interval of 20–1400 °C was reduced by 3.3 wt.%, indicating almost complete decomposition of the organometallic complex. The main weight reduction (3 wt.%) for the SDC-3 is in the range of 20–465 °C. This is usually associated with the removal of residual water (endothermic effect at ~65 °C) and the oxidation of residual organic particles (exothermic effect in 370 °C) [35,56]. In the case of BCS-3 powder several stages of mass loss are observed. The first stage is characterized by a change of 2.4 wt.% upon heating from room temperature up to 350 °C and is associated with the partial

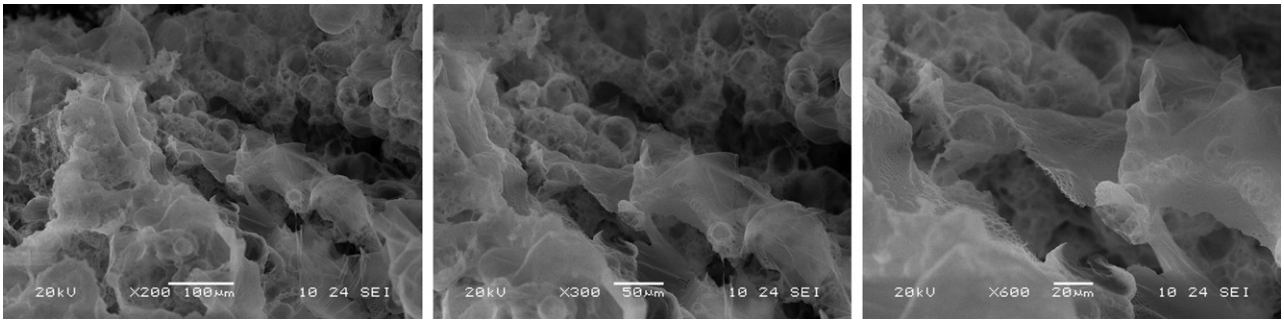

Fig. 1. SEM images of as-prepared by SCS method 7SDC-3BCS-1 powder with different magnitude.

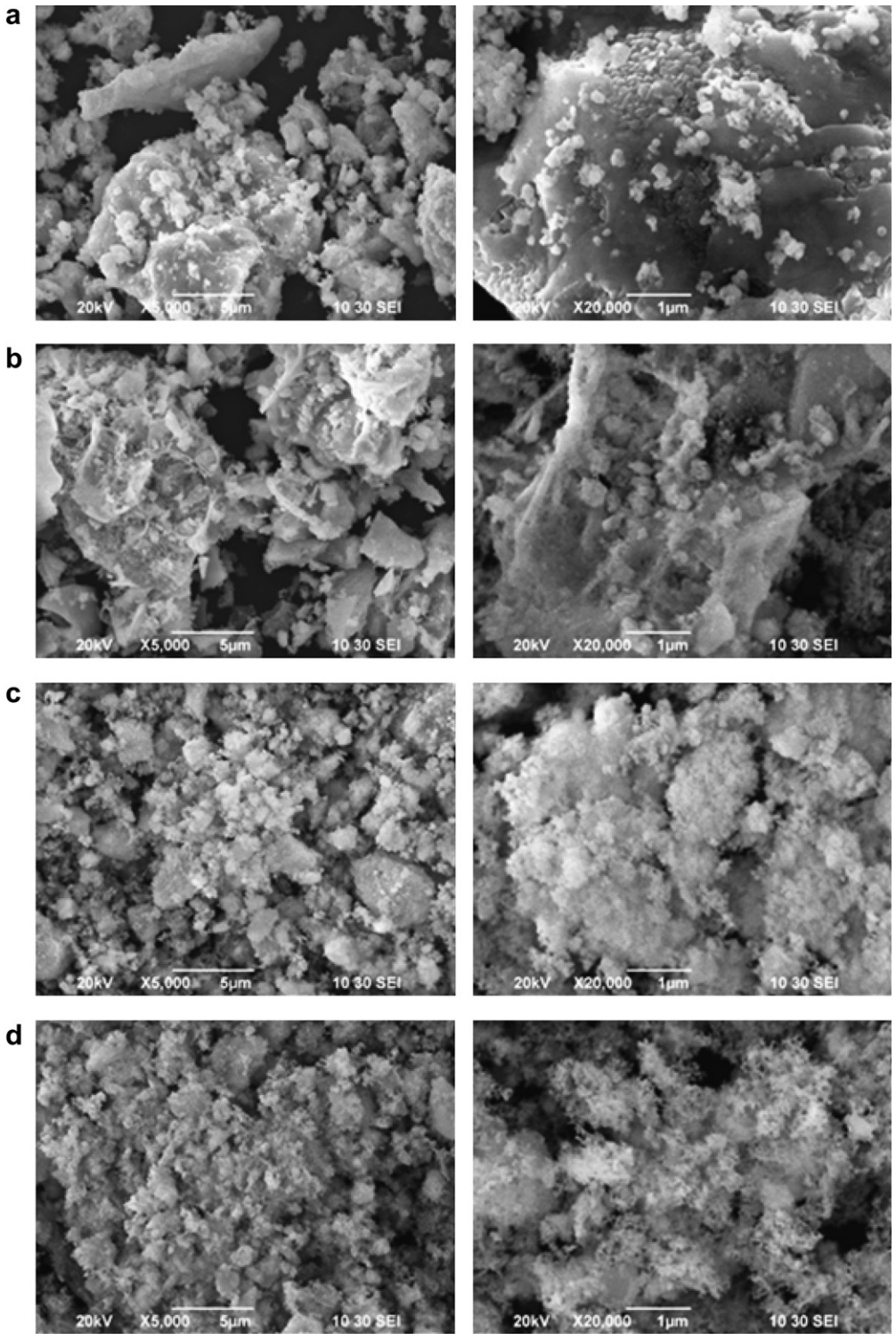

Fig. 2. The SEM image of morphology of (a) 7SDC–3BCS-1, (b) 7SDC–3BCS-2, (c) 7SDC–3BCS-3 and (d) 7SDC–3BCS-4 annealed powders obtained by SCS method (with two different magnitudes).

removal, as in the case of SDC-3 powder, of water and adsorbed particles on the powder's surface. The significant change in the weight (6.9 wt.% in the temperature interval 400–650 °C) is the result of the oxidation of organic particles and the subsequent removal of CO_2, N_2 and H_2O [22]. The final stage of mass loss, starting at 800 °C is related with the decomposition of barium carbonate [57], which is, apparently, an intermediate substance in the following scheme of transformation: $Ba(NO_3)_2 \rightarrow BaCO_3 \rightarrow ''BaO'' \rightarrow BaCeO_3$. The small endothermic reflex at 830 °C is connected with a phase transition of barium carbonate from orthorhombic (γ-$BaCO_3$, space group Pmcn) to tetragonal structure (β-$BaCO_3$, space group $R\bar{3}m$) [58,59]. In the case of the 7SDC–3BCS-3 composite, a behavior of the curves similar to BCS-3 is observed. For all the compounds during heating at 1080 °C, no changes in the mass of the powders were

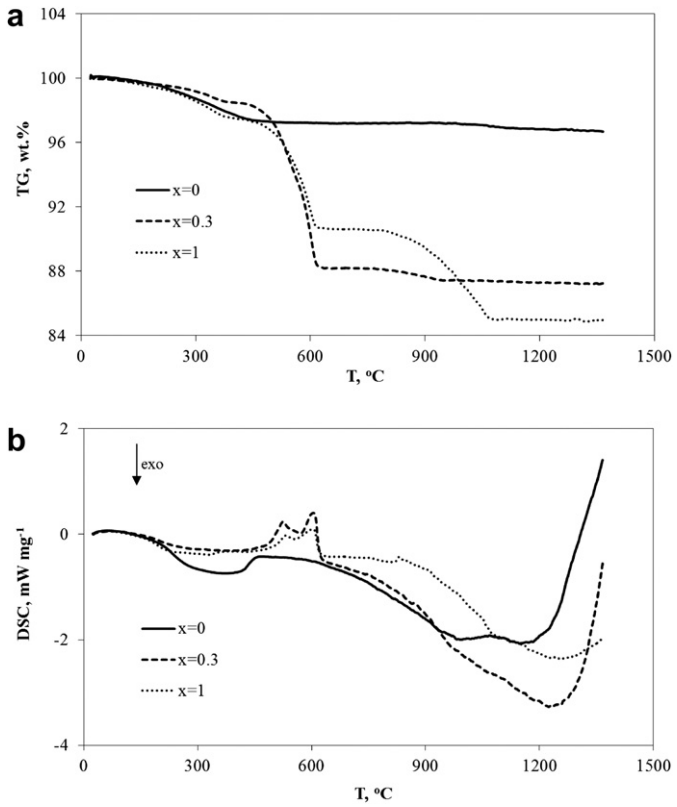

Fig. 3. (a) TG and (b) DSC curves of as combusted $(1-x)Ce_{0.8}Sm_{0.2}O_{2-\delta}$–$xBaCe_{0.8}Sm_{0.2}O_{3-\delta}$ powders as-prepared by SCS method with glycerin as a fuel.

detected. Apparently, this is due to the end of the decomposition process and the formation of the perovskite and/or fluorite phase.

To confirm the TG-DSC analysis, we performed XRD analysis of the BCS-3 powder calcined at 500, 700, 900 and 1100 °C for 3 h (Fig. 4). The presented data show that in the range of 500–900 °C the powder is not single-phase. In addition to the perovskite phase, the presence of phases based on barium carbonate, cerium oxide and undetected phase are observed. For the BCS-3 powder calcined at 1100 °C, no additional reflections corresponding to impurity phases were detected. Based on these data, all powders of $(1-x)Ce_{0.8}Sm_{0.2}O_{2-\delta}$–$xBaCe_{0.8}Sm_{0.2}O_{3-\delta}$ were calcined at 1100 °C for 3 h.

Fig. 5 shows the room temperature XRD data of $(1-x)Ce_{0.8}Sm_{0.2}O_{2-\delta}$–$xBaCe_{0.8}Sm_{0.2}O_{3-\delta}$ powders obtained with

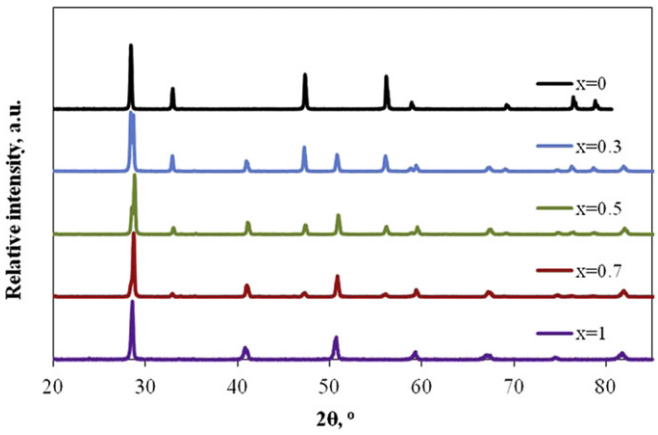

Fig. 5. Room temperature XRD patterns of $(1-x)Ce_{0.8}Sm_{0.2}O_{2-\delta}$–$xBaCe_{0.8}Sm_{0.2}O_{3-\delta}$ powders prepared by SCS method with glycerin and calcined at 1100 °C for 3 h.

glycerin and synthesized at 1100 °C. According to the presented data, SDC-3 crystallizes in the cubic fluorite-type structure (space group $Fm\bar{3}m$) and BCS-3 in the orthorhombic perovskite structure (space group Pmcn). For $(1-x)Ce_{0.8}Sm_{0.2}O_{2-\delta}$–$xBaCe_{0.8}Sm_{0.2}O_{3-\delta}$-3 powders ($x = 0.3, 0.5, 0.7$) two different phases were found; the main characteristic reflections which correspond to the structure of fluorite and perovskite. The XRD patterns show that no additional reflections related to the impurity phases as in the base compositions (SDC and BCS), as composites (SDC–BCS) were observed.

As it was noted in the introduction part, $BaCeO_3$ based materials are destroyed in CO_2 and H_2O- containing atmosphere and the increase of the fluorite content in the system can improve the stability of the composite materials. As shown in Fig. 6, $0.5Ce_{0.8}Sm_{0.2}O_{2-\delta}$–$0.5BaCe_{0.8}Sm_{0.2}O_{3-\delta}$-3 powders after exposure at $CO_2 + H_2O$ atmosphere (750 °C for 10 h) are relatively stable and small reflexes that correspond to impurity phases are detected. On the contrary, the $BaCe_{0.8}Sm_{0.2}O_{3-\delta}$-3 and $0.3Ce_{0.8}Sm_{0.2}O_{2-\delta}$–$0.7BaCe_{0.8}Sm_{0.2}O_{3-\delta}$-3 samples were destroyed indicating a weak chemical stability of these powders.

In Fig. 7 the XRD patterns of 7SDC–3BCS powder compositions obtained with different fuels and calcined at 1100 °C are shown. It was found that single-phase powders formation of double composition occurs, regardless of the type of the used fuel. Thus, the single-stage combustion of the precursors is a suitable method for the production of $(1-x)Ce_{0.8}Sm_{0.2}O_{2-\delta}$–$xBaCe_{0.8}Sm_{0.2}O_{3-\delta}$ composites.

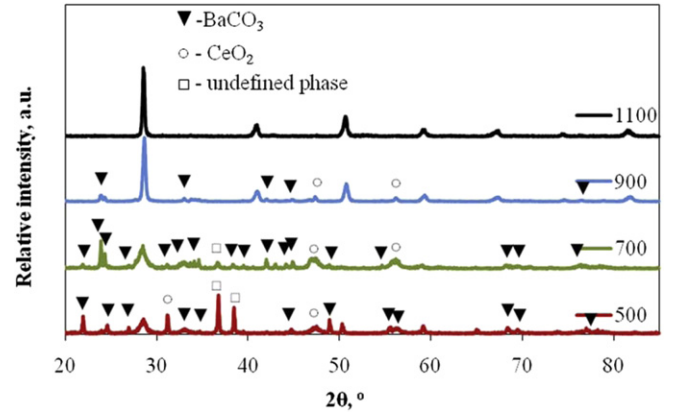

Fig. 4. Room temperature XRD patterns of the BCS-3 powders calcined at 500, 700, 900 and 1100 °C for 3 h.

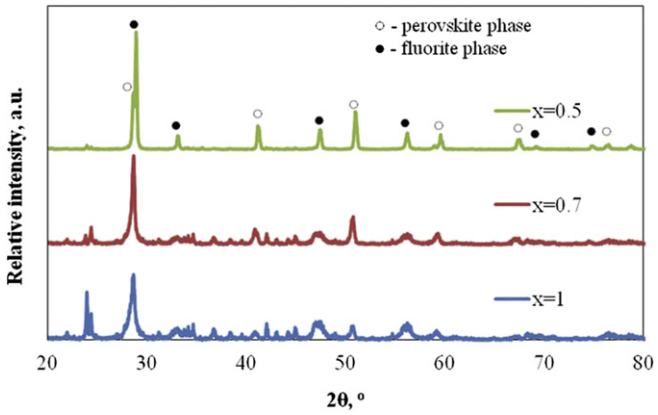

Fig. 6. Room temperature XRD patterns of $(1-x)Ce_{0.8}Sm_{0.2}O_{2-\delta}$–$xBaCe_{0.8}Sm_{0.2}O_{3-\delta}$-3 powders after exposure in 97 vol.% $CO_2 + 3$ vol.% H_2O atmosphere at 750 °C for10 h.

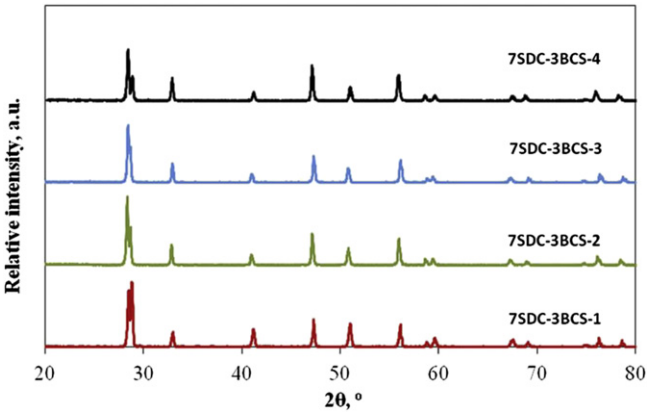

Fig. 7. Room temperature XRD patterns of $0.7Ce_{0.8}Sm_{0.2}O_{2-\delta}$–$0.3BaCe_{0.8}Sm_{0.2}O_{3-\delta}$ powders calcined at 1100 °C for 3 h.

In Table 2 the structural parameters of the calcined nano-sized powders are listed. It can be seen that the lattice parameters for the SDC-3 and the BCS-3 are in good agreement with literature data [50,60–62]. In addition, for $(1-x)Ce_{0.8}Sm_{0.2}O_{2-\delta}$–$xBaCe_{0.8}Sm_{0.2}O_{3-\delta}$ powders prepared by glycerin-nitrate technique, the lattice parameters of each phase were obtained. It can be seen that the unit cell volume of the fluorite phase in the composite materials does not change monotonically; however, a slight increase of its volume with the increase of x can be observed. At the same time, the unit cell volume of the perovskite phase is increased. The change of the crystal parameters can be connected with cations' diffusion arising due to the different chemical potential of ions between perovskite and fluorite phases. Most likely, the diffusion of barium ions from barium cerate to Sm-doped ceria. However, the solubility of Ba^{2+} in Ce^{4+} sublattice is limited to 2 mol.% [35] and, correspondingly, cannot result in a strong change of the unit cell parameters. The second reason for the aforementioned phenomenon may be a partial diffusion of Sm^{3+}-ions from perovskite to fluorite phase. But in this case, the lattice parameters of the ceria system are strongly dependent on the amount of the acceptor-dopant [63] and the change of the unit cell parameters shows no significant variation of Sm^{3+} concentration in the fluorite phase. It can be concluded that the ion deviation from the stoichiometric value of the perovskite and fluorite systems is slight. In the work of Venkatasubramanian et al. [40] the reverse tendency for perovskite system is observed. The decrease of the lattice parameters of barium cerate phase with the increase of x in $(1-x)Ce_{0.8}Gd_{0.2}O_{2-\delta}$–$xBaCe_{0.8}Gd_{0.2}O_{3-}$ $(0 \le x \le 0.4)$ composite system, is attributed by the authors to the partial substitution of Ba^{2+} by Gd^{3+}.

The size of the crystallites (D_{hkl}) affects both the fuel and the maintenance of barium cerate in the composite. The presented data show that the crystallite size increases with the increase of the perovskite phase content in the $(1-x)Ce_{0.8}Sm_{0.2}O_{2-\delta}$–$xBaCe_{0.8}Sm_{0.2}O_{3-\delta}$ system obtained with glycerin from 17.2 nm ($x=0$) to 50.2 nm ($x=1$). This result is in contradiction with the theoretical ideas concerning the method of SCS, as the analysis of reaction (1) shows that the increase of the x content in this system (using one type of fuel) results in an increase in the number of gaseous substances, which should lead to a more intense dispersion of oxides and to the formation of more fine powders [55]. On the other hand, it is known that an increase in the lattice parameters of the solid solution results in the growth of crystallite size for the submicron materials [64]. Since the size of the perovskite unit cell is greater than fluorite, our patterns with changes in the structure are well described by taking into account the size factor.

The particle sizes determined by Scherrer's equation for all samples are smaller than that of the crystallite size determined by BET, which is associated with the process of agglomeration. The degree of agglomeration (D_{BET}/D_{hkl}) increases with the decrease in the amount of fluorite phases in the system $(1-x)Ce_{0.8}Sm_{0.2}O_{2-\delta}$–$xBaCe_{0.8}Sm_{0.2}O_{3-\delta}$ from 1.47 to 4.21 at $x=0$ and 1, respectively (fuel glycerin). The D_{BET}/D_{hkl} ratio was also significantly affected by the type of the fuel. The degree of agglomeration for 7SDC–3BCS powder obtained by SCS with glycine is very high (8.89), whereas the use of glycerin or a mixture of citric acid and ethylene glycol leads to reduced degree of agglomeration to 1.36 and 3.54, respectively. It should be noted that the crystallite size of the particles and powders obtained in this study are somewhat lower in the literature. This result can be explained by the fact that the powders prepared by SCS in the present study were obtained at strictly stoichiometric amount of fuel, while in the works [50,60–62] the oxide powders were obtained with a significant excess of an organic agent.

In order to select the optimum temperature for obtaining gastight ceramics from nano-sized powders, a comparative study of the sintering kinetics of the base material and composite material obtained from glycerin was investigated. Fig. 8 shows the curves of shrinkage ($\Delta l/L$) and the rate of linear change [$d(\Delta l/L)/dt$] of the samples in the temperature range of 20–1500 °C. The data show that the shrinkage of the 7SDC–3BCS-3 and SDC-3 samples begins at fairly low temperatures (300–400 °C). The maximum rate of change of linear dimensions for these materials is implemented at 1200 °C and ends at 1465 and 1370 °C, respectively, which indicates the completion of the sintering process. The relative change of the linear dimensions of 7SDC–3BCS-3 and SDC-3 samples at these temperatures is approximately 25%. The nature of the shrinkage of the sample BCS-3 is somewhat different. A significant change in the linear dimensions for this material begins at 1000 °C, with the first expansion occurring in the temperature range of 1000–1100 °C, and then shrinking from 1100 to 1500 °C, which is consistent with

Table 2
Crystal parameters, particle and crystallite size of $(1-x)Ce_{0.8}Sm_{0.2}O_{2-\delta}$–$xBaCe_{0.8}Sm_{0.2}O_{3-\delta}$ powder materials calcined at 1100 °C.

Materials	Perovskite phase				Fluorite phase		D_{hkl}, nm	D_{BET}, nm	References
	a, Å	b, Å	c, Å	V, Å^3	a, Å	V, Å^3			
SDC					5.427	159.84	5.42	16.2	[50]
SDC					5.433	160.37	9.2	25.7	[60]
BCS	8.771	6.264	6.228	342.18					[61]
BCS	8.798	6.247	6.227	342.24					[62]
SDC-3					5.436	160.63	17.2	25.2	Present work
7SDC–3BCS-3	8.781	6.246	6.225	341.42	5.438	160.81	18.5	25.2	
5SDC–5BCS-3	8.779	6.247	6.226	341.46	5.437	160.72	25.3	32.7	
3SDC–7BCS-3	8.785	6.250	6.228	341.96	5.439	160.90	34.1	50.4	
BCS-3	8.796	6.249	6.226	342.22			50.2	211.2	
7SDC-3BCS-1							30.3	269.5	
7SDC-3BCS-2							21.8	110.2	
7SDC-3BCS-4							20.1	71.1	

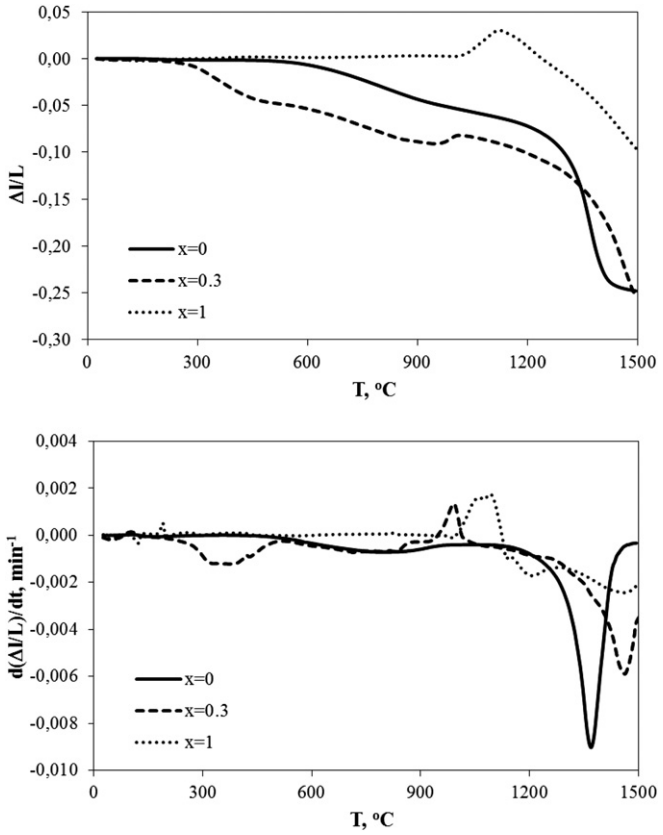

Fig. 8. Dilatometric curves of the pressed pellets from the calcined and ball-milled $(1-x)Ce_{0.8}Sm_{0.2}O_{2-\delta}$–$xBaCe_{0.8}Sm_{0.2}O_{3-\delta}$-3 powders.

the results of Chien et al. [52] and Koferstein et al. [65]. The maximum change in the linear dimensions of BCS-3 sample is 9%; probably, the temperature of 1500 °C is insufficient to complete the process of sintering of the specific material. Thus, with increasing the content of barium cerate system $(1-x)Ce_{0.8}Sm_{0.2}O_{2-\delta}$–$xBaCe_{0.8}Sm_{0.2}O_{3-\delta}$ the ceramic sintering temperature increases.

Fig. 9 shows the micrographs of the surface morphology of the unpolished samples SDC-3, BCS-3 and the composite 7SDC–3BCS-(1-4) sintered at 1500 °C for 3 h. The surface of all samples except for BCS-3 is characterized by well-formed grains and free-pore structure. It should be noted that the grain size depends on the prehistory of the calcined powders and the sintered ceramics. In the case of 7SDC–3BCS-1 the grain size is equal to 2–15 μm with predominance of large particles, whereas in the case of 7SDC–3BCS-3 is ~1 to 4 μm. The structure of the BCS-3 sample's surface is porous. The relative density determined by hydrostatic weighing in kerosene for composite samples and ceramics based on cerium oxide is 94–97%, whereas for the barium cerate sample – 91% of the theoretical.

In order to confirm the phase composition of the composite after sintering, XRD analysis was performed for the crushed ceramic into powder and SEM study of the cross-section morphology of 7SDC–3BCS-3 ceramic sample. According to the XRD analysis, the content of barium cerate phase in the powder was 53.5 ± 5.4 wt.% and slightly higher than the theoretical calculated for 7SDC–3BCS-3 (44.7 wt.%). The crystal parameters for the perovskite and fluorite phases in the composite are $8.795 \times 6.247 \times 6.220$ Å^3 and 5.437 Å, respectively, and differ slightly from the parameters listed in Table 2 for the calcined 7SDC–3BCS-3 powder. This result confirms that the elemental composition for each phase of the calcined and sintered materials is consistent with the nominally specified. Fig. 10 shows the distribution of the main elements of the cross-section of the ceramic sample 7SDC–3BCS-3. From the micrographs, it is clear that almost all elements are uniformly distributed over the volume of the sample and no individual grains with micron size related to the phase of barium cerate or cerium oxide were observed. This result may indicate that the distribution of the two phases is not at the micro level (such as in [42]), but at the submicron level (such as in [41]).

Fig. 11 shows the dilatometric data for $(1-x)Ce_{0.8}Sm_{0.2}O_{2-\delta}$–$xBaCe_{0.8}Sm_{0.2}O_{3-\delta}$ ceramic samples in air. The graph shows that for barium cerate and the composite with $x = 0.7$ the change in the slope at 550–650 °C is observed, which may be associated with a higher symmetry of the perovskite structure. A similar trend is noted in the works of Ohzeki et al. [38] and Knight [66] for undoped barium cerate, for which the perovskite structure at $T > 400$ °C changes from orthorhombic (space group Imma) to rhombohedral (space group $R\bar{3}m$) and at $T \approx 895$ °C from rhombohedral to cubic (space group $Pm\bar{3}m$). The temperature dependence of the expansion for SDC-3 and the composite with $x = 0.3$ and 0.5 is not characterized by a sharp change in linear dimensions. Table 3 shows the values of TEC calculated by the linear plots of $\Delta l/L$–T dependence. The presented data show that for SDC sample the TEC is 12.4×10^{-6} K^{-1} and is consistent with literature data [67–69]. In the case of the BCS-3 sample TEC designed in the range of 650–900 °C is equal to 10.5×10^{-6} K^{-1} and agrees with the TEC data of the some materials based on $BaCeO_3$ [70–72]. It should be noted that with the increase of flourite-content in $Ce_{0.8}Sm_{0.2}O_{2-\delta}$–$BaCe_{0.8}Sm_{0.2}O_{3-\delta}$ system, the TEC value of the ceramic sample is weakly increased and the change in the slop of the thermal expansion curves at 550–650 °C is smoother. Similar TEC values of SDC and BCS materials are favorable for the use of SDC–BCS composite ceramics as an electrolyte in electrochemical devices at various technological processes (heating, cooling and cycling).

The dependences of the total conductivity values in Arrhenius coordinates for $(1-x)Ce_{0.8}Sm_{0.2}O_{2-\delta}$–$xBaCe_{0.8}Sm_{0.2}O_{3-\delta}$ samples prepared by SCS method with glycerin are presented in Fig. 12 (wet air atmosphere). The graph shows that the conductivity of the sample based on cerium dioxide at the high-temperature range ($T > 600$ °C) is higher than that of the sample based on barium cerate, while at the low-temperature range there is an opposite trend. This can be explained by the different activation energy of conductivity (in our work for the SDC-3 it is 0.73 and 0.80 eV for low-and high-temperature region, respectively, whereas for the BCS-3 it is 0.41 and 0.66 eV, respectively). The calculated activation energies are in good agreement with literature data for both samples based on $Ce_{0.8}Sm_{0.2}O_{2-\delta}$ [73–75] and for $BaCe_{0.8}Sm_{0.2}O_{3-\delta}$ [62,76]. The lower values of activation energy of the materials based on barium cerate are, apparently, related with the presence of proton conductivity in humid air, which at relatively low temperatures is the dominant charge carrier of the oxide [64]. The conductivity of the $(1-x)Ce_{0.8}Sm_{0.2}O_{2-\delta}$–$xBaCe_{0.8}Sm_{0.2}O_{3-\delta}$ composite ceramic samples is lower than that of the SDC-3 in the high-temperature region and lower than that of BCS-3 at the low-temperature region. This behavior of conductivity indicates that the transport processes take place mainly through the phase whose content in the composite is predominant (partial effect of conductivities). This tendency is observed in the work of Venkatasubramanian et al. [40] where the total conductivity of the $xBaCe_{0.8}Gd_{0.2}O_{3-\delta}$–$(1-x)Ce_{0.8}Gd_{0.2}O_{3-\delta}$ samples ($x = 0$, 0.1, 0.2, 0.3, 0.4) at 600–800 °C (high-temperature region) in air decreases with the increase of x, suggesting that the contribution from the BCG–CG interface increases with the increase of BCG volume fraction. Moreover, in the work of Khandelwal et al. [42] the conductivities of the composite materials at 400–500 °C (low-

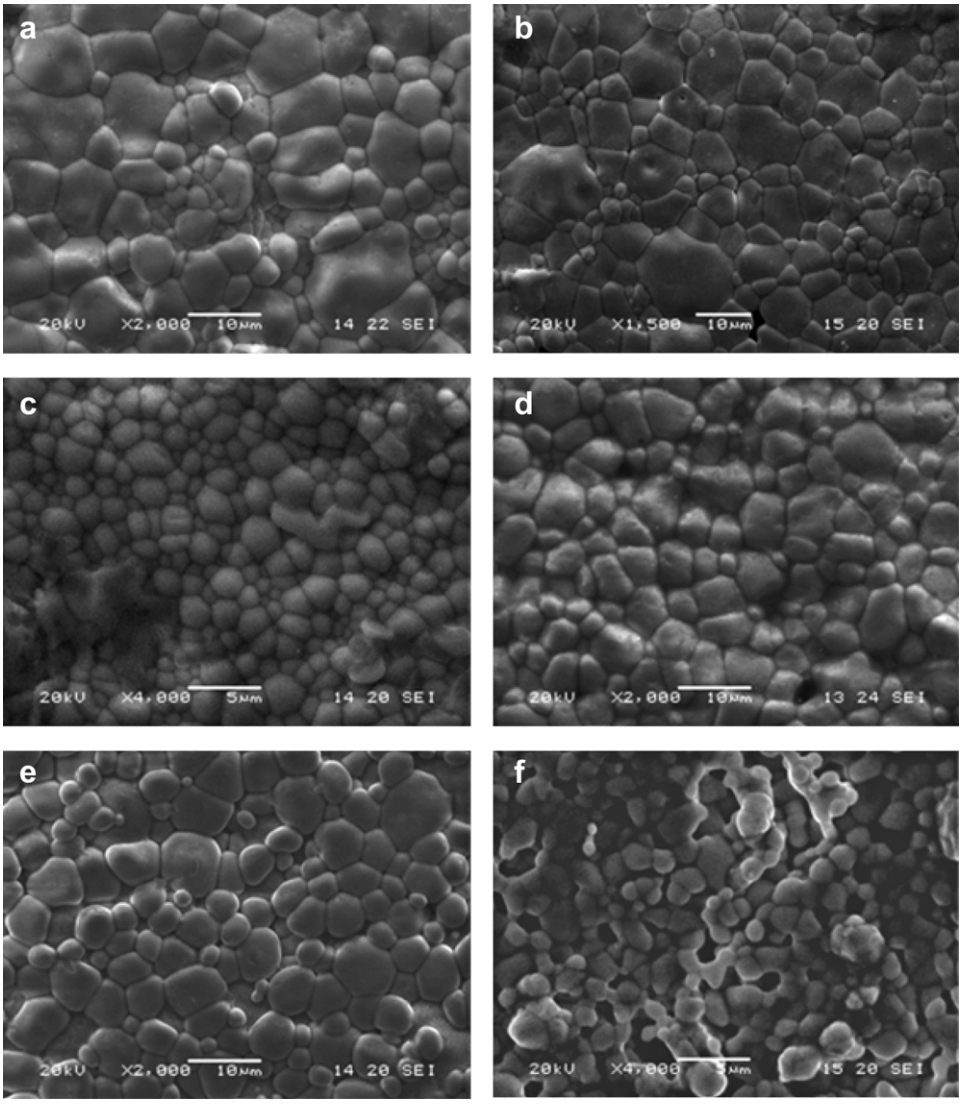

Fig. 9. SEM images of (a) 7SDC−3BCS-1, (b) 7SDC−3BCS-2, (c) 7SDC−3BCS-3, (d) 7SDC−3BCS-4, (e) SDC−3 and (f) BCS-3 surface samples sintered at 1500 °C for 3 h.

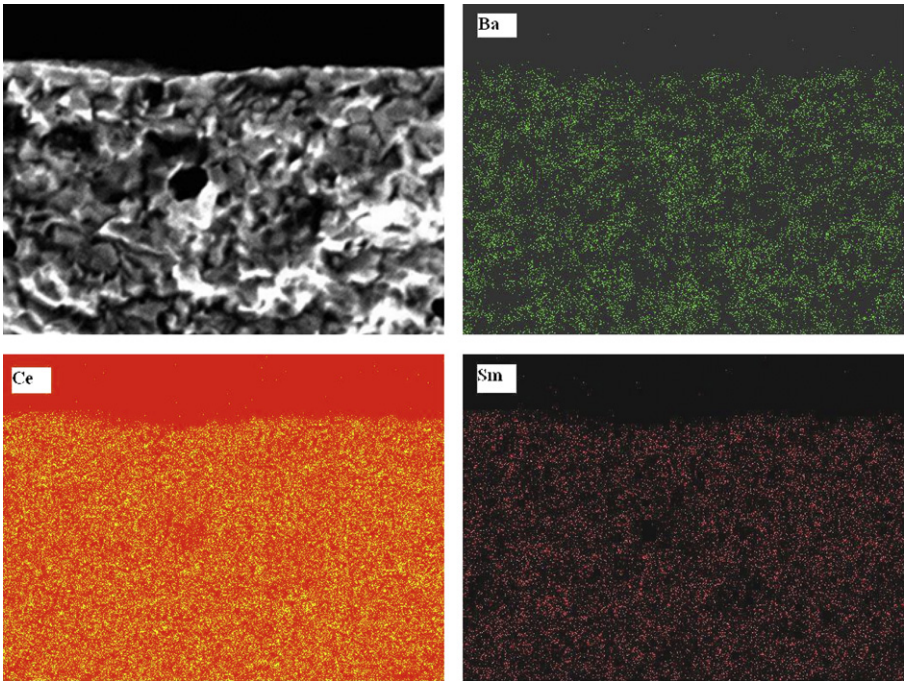

Fig. 10. SEM images and element distribution of fracture cross-section of 7SDC−3BCS-3 ceramic sample sintered at 1500 °C for 3 h.

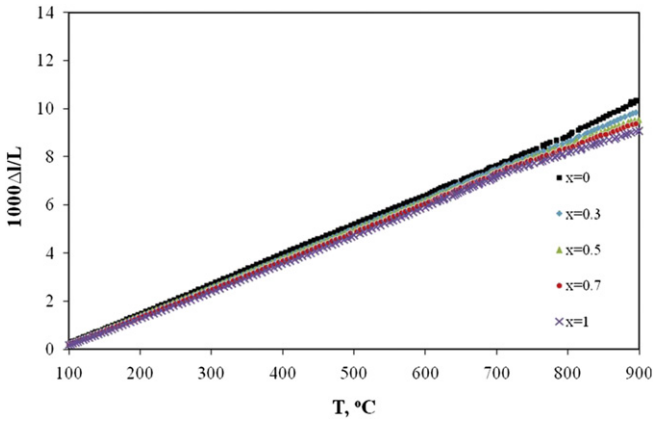

Fig. 11. Thermal expansion behavior of $(1-x)Ce_{0.8}Sm_{0.2}O_{2-\delta}$–$xBaCe_{0.8}Sm_{0.2}O_{3-\delta}$-3 ceramics in air.

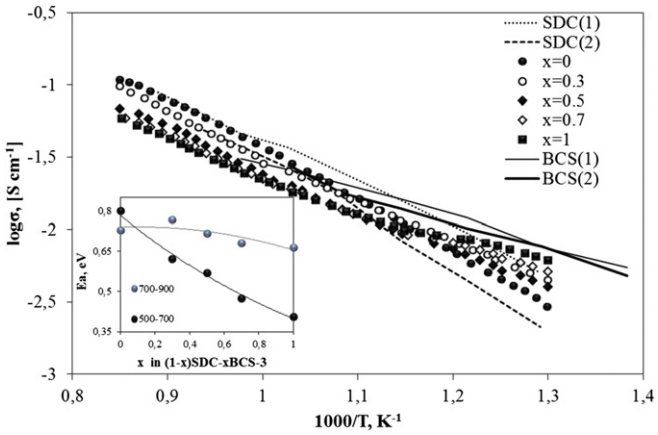

Fig. 12. Temperature dependences of electrical conductivity for $(1-x)Ce_{0.8}Sm_{0.2}O_{2-\delta}$–$xBaCe_{0.8}Sm_{0.2}O_{3-\delta}$-3 ceramic samples in wet air. Insert: concentration dependences of Ea for the samples of this system at 500–700 and 700–900 °C. The data for SDC(1) are taken from [79], for SDC(2) from [80], for BCS(1) from [62] and BCS(2) from [61].

temperature region) are lower than those of $BaCe_{0.85}Gd_{0.15}O_{3-\delta}$ sample and higher than those of $Ce_{0.8}Gd_{0.2}O_{2-\delta}$. It should be noted that in [40] the conductivity of the $xBaCe_{0.8}Gd_{0.2}O_{3-\delta}$–$(1-x)Ce_{0.8}Gd_{0.2}O_{3-\delta}$ composite ceramics is lower compared to $BaCe_{0.85}Gd_{0.15}O_{3-\delta}$ as $Ce_{0.8}Gd_{0.2}O_{3-\delta}$ samples at the whole temperature range and is contradiction with our data. This contradiction can be explained by the different values of bulk and grain boundary conductivities (not measured in this work). We suggest that SCS method standard compared to solid state method is more favorable for uniform element distribution and leads to enhanced conductivity of composite ceramics concerning BCS and SDC samples in high- and low-temperature interval, respectively [49]. The values of activation energy (Ea) of conductivity were calculated from the equation:

$$\sigma T = A \cdot \exp[-E_a/RT] \quad (5)$$

and are presented in the insert of Fig. 12. It can be seen that activation energy decreases with increasing x in $(1-x)Ce_{0.8}Sm_{0.2}O_{2-\delta}$–$xBaCe_{0.8}Sm_{0.2}O_{3-\delta}$ system. The observed behavior is in agreement with literature data, well-known that systems based on cerium oxide present higher values of activation energy than systems based on barium cerate [77–80]. In addition, the change of Ea with the increase of x at the high-temperature region is smaller than that at the low-temperature region. This can be explained by the fact that at 700–900 °C in wet air the conductivity of $(1-x)Ce_{0.8}Sm_{0.2}O_{2-\delta}$–$xBaCe_{0.8}Sm_{0.2}O_{3-\delta}$ ceramic samples is predominantly ionic for low x or mixed ionic-electronic (p-type) for high x. The change of perovskite content in the composite system has a negligible impact on the change of Ea due to the comparable level of Ea for oxygen-ion and hole conductivities. On the contrary, barium cerate based materials at 500–700 °C in wet atmosphere are characterized predominantly by proton conductivity with activation energy lower than those for oxygen-ion and hole conductivities. Correspondingly, with the increase of perovskite phase in $(1-x)Ce_{0.8}Sm_{0.2}O_{2-\delta}$–$xBaCe_{0.8}Sm_{0.2}O_{3-\delta}$ system, the value of activation energy in the low-temperature interval will decrease, as observed in our case.

Table 3
TEC value of samples based on cerium oxide, barium cerate and their composites.

Type	Sample	Temperature interval, °C	$\alpha \times 10^6$, K^{-1}	References
Fluorite	SDC-3	20–900	12.4	Present work
	SDC	350–900	12.3	[67]
	SDC	25–800	12.6	[68]
	SDC	–	12.8	[69]
Perovskite	BCS-3	100–500	11.5	Present work
		620–900	10.3	
	BCS	600–900	9.3	[70]
	$BaCe_{0.8}Gd_{0.2}O_{3-\delta}$	20–1000	9.8	[71]
	$BaZr_{0.1}Ce_{0.7}Y_{0.1}Yb_{0.1}O_{3-\delta}$	100–500	14.2	[72]
		600–700	5.4	
		800–1100	11.6	
Composite	7SDC–3BCS-3	20–900	12.1	Present work
	5SDC–5BCS-3	20–900	11.8	Present work
	3SDC–7BCS-3	100–600	11.7	Present work
		600–900	11.1	

Finally, the conductivity as a function of pO_2 for the samples of $(1-x)Ce_{0.8}Sm_{0.2}O_{2-\delta}$–$xBaCe_{0.8}Sm_{0.2}O_{3-\delta}$-3 system was measured (Fig. 13). According to the obtained results, the two-phase samples have a wider electrolytic domain boundary (the area where the ion conductivity is higher that electron conductivity) than those of the individual single-phase materials. At this point, the 0.5SDC–0.5BCS-3 ceramic sample is characterized by the lowest values of partial n- and p-type electron conductivities independent on temperature. These qualitative data are in agreement with quantitative results which have been obtained according to the following equation [64,81–83]:

$$\sigma = \sigma_i + \sigma_{p,o} \cdot pO_2^{1/4} + \sigma_{e,o} \cdot pO_2^{-1/4}, \quad (6)$$

where $\sigma_{p,o}$ and $\sigma_{e,o}$ are the values of electron conductivity of p- and n-type at $pO_2 = 1$ atm, respectively, and σ_i = const the ionic conductivity.

The data obtained by fitting theoretical model corresponding to Eq. (6) with experimental results are presented in Table 4. It can be seen that n-type conductivity decreases and p-type conductivity increases with increasing x in $(1-x)Ce_{0.8}Sm_{0.2}O_{2-\delta}$–$xBaCe_{0.8}Sm_{0.2}O_{3-\delta}$ system. From this viewpoint, $0.5Ce_{0.8}Sm_{0.2}O_{2-\delta}$–$0.5BaCe_{0.8}Sm_{0.2}O_{3-\delta}$ ceramic sample has the highest ionic contribution to the total conductivity in both oxidizing and reducing atmospheres. It should be also noted that the ionic conductivity of the samples enriched by fluorite phase is higher than those enriched by perovskite phase. However, the decrease of temperature leads to a decrease of ionic conductivity differences between the individual materials: at 900 °C the ionic conductivity of $Ce_{0.8}Sm_{0.2}O_{2-\delta}$ sample is 4.4 times greater than the

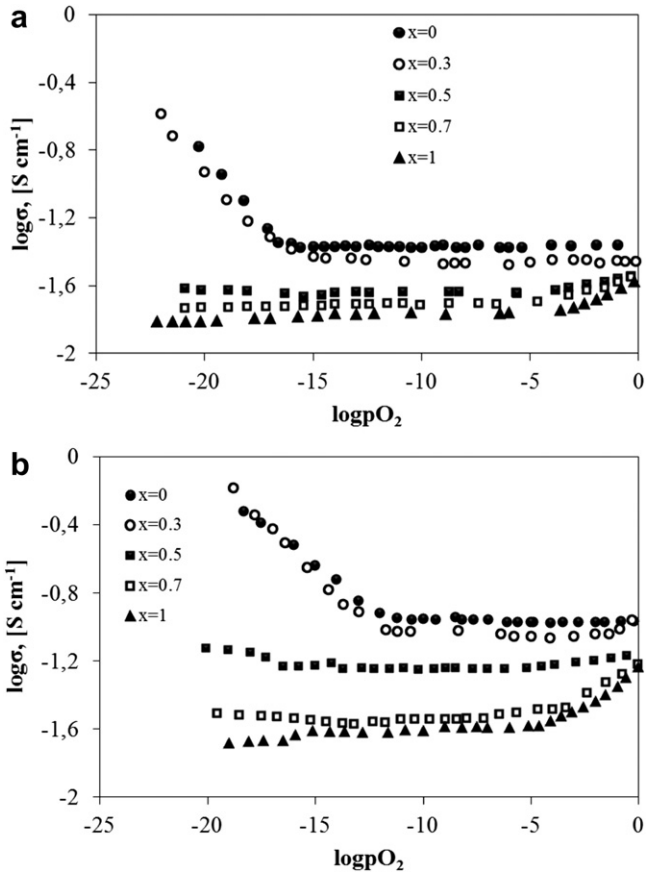

Fig. 13. Oxygen partial pressure dependency of the total conductivity for $(1-x)Ce_{0.8}Sm_{0.2}O_{2-\delta}$–$xBaCe_{0.8}Sm_{0.2}O_{3-\delta}$-3 ceramic samples at 750 °C (a) and 900 °C (b).

$Ce_{0.8}Sm_{0.2}O_{2-\delta}$–$xBaCe_{0.8}Sm_{0.2}O_{3-\delta}$ ($x \neq 0$ and 1) prepared by single-stage method from the nitrates consist of two-phases without any traces of other impurities. The influence of the fuel and the content of barium cerate in the system $(1-x)Ce_{0.8}Sm_{0.2}O_{2-\delta}$ $-xBaCe_{0.8}Sm_{0.2}O_{3-\delta}$ on the morphology of the obtained powders and ceramic samples were investigated. It was found that the most nano-sized powders and gastight ceramics with fine grain structure are obtained for $x = 0$ ($Ce_{0.8}Sm_{0.2}O_{2-\delta}$) using glycerin. The conductivity of the $(1-x)Ce_{0.8}Sm_{0.2}O_{2-\delta}$–$xBaCe_{0.8}Sm_{0.2}O_{3-\delta}$ ($x \neq 0$ and 1) composite materials is determined by the phase, the content of which is more in this fluorite-perovskite system. The $0.5Ce_{0.8}Sm_{0.2}O_{2-\delta}$–$0.5BaCe_{0.8}Sm_{0.2}O_{3-\delta}$ material can be recommended for use as an electrolyte for intermediate and high temperature electrochemical devices due to the relatively good stability in CO_2-containing atmospheres, similar values of component's TEC and low contribution of the electron (n- and p-type) conductivity to the total conductivity in a wide temperature range. Moreover, the composites based on cerium oxide and barium cerate can be used not only as electrolytes, but also as components of multiphase composite cathodes, for example, $La_{0.8}Sr_{0.4}Co_{0.2}Fe_{0.8}O_{3-\delta}$ $-BaCe_{0.8}Y_{0.2}O_{3-\delta}$–$Ce_{0.8}Gd_{0.2}O_{2-\delta}$ [49] and $Sm_{0.5}Sr_{0.5}CoO_{3-\delta}$–$Ce_{0.8}$ $Sm_{0.2}O_{2-\delta}$–$BaZr_{0.1}Ce_{0.7}Y_{0.2}O_{3-\delta}$ [85].

Acknowledgments

The present work was financially supported concerning the authors affiliated at Institute of High Temperature Electrochemistry by the Russian Foundation for Basic Research (12-08-31005 мол-а), the Ministry of Education and Science of the Russian Federation (contract number 16.516.12.6003) and the Research Program of the Presidium of RAS (project No. 12-П-23-2006). Finally, Prof. P. Tsiakaras is grateful to the Greek Ministry of Development-GSRT "SYNERGASIA" Program (09SYN-32-615: ECHOCO2) for the financial support.

Table 4
Parameters of the Eq. (6) for the $(1-x)Ce_{0.8}Sm_{0.2}O_{2-\delta}$–$xBaCe_{0.8}Sm_{0.2}O_{3-\delta}$–3 ceramic samples.

Samples	750 °C			900 °C		
	$\sigma_{e,o}$, S cm^{-1}	σ_i, S cm^{-1}	$\sigma_{p,o}$, S cm^{-1}	$\sigma_{e,o}$, S cm^{-1}	σ_i, S cm^{-1}	$\sigma_{p,o}$, S cm^{-1}
BCS-3	$<10^{-7}$	1.7×10^{-2}	1.1×10^{-2}	$<10^{-7}$	2.5×10^{-2}	3.3×10^{-2}
3SDC–7BCS-3	$<10^{-7}$	1.9×10^{-2}	1.2×10^{-2}	2.7×10^{-6}	2.7×10^{-2}	4.2×10^{-2}
5SDC–5BCS-3	8.0×10^{-6}	2.2×10^{-2}	8.8×10^{-3}	8.6×10^{-6}	5.7×10^{-2}	1.7×10^{-2}
7SDC–3BCS-3	4.9×10^{-5}	3.4×10^{-2}	1.1×10^{-3}	4.2×10^{-4}	8.7×10^{-2}	2.8×10^{-3}
SDC-3	5.1×10^{-5}	4.4×10^{-2}	$<10^{-7}$	3.3×10^{-4}	11.0×10^{-2}	$<10^{-7}$

conductivity of $BaCe_{0.8}Sm_{0.2}O_{3-\delta}$ sample and at 750 °C – only 2.6 times. It is obvious that at intermediate temperatures, their ionic conductivity can be equal, and at low-temperature range, according to the literature data [77,78], the ionic conductivity of barium cerate is higher than that of cerium oxide. The table data show that the co-presence of perovskite and fluorite phases leads to electronic current-blocked effect suggested in the works of Sun et al. [41,84].

4. Conclusions

In the present work nano-sized powders of $(1-x)$ $Ce_{0.8}Sm_{0.2}O_{2-\delta}$–$xBaCe_{0.8}Sm_{0.2}O_{3-\delta}$ were prepared by solution combustion synthesis (self-combustion synthesis, SCS) method using different types of fuels. It was determined that the phase structure of the individual oxides $Ce_{0.8}Sm_{0.2}O_{2-\delta}$ and $BaCe_{0.8}Sm_{0.2}O_{3-\delta}$ corresponds to the fluorite and perovskite structure, respectively. The composite materials of $(1-x)$

References

[1] N.Q. Minh, T. Takahashi, Science and Technology of Ceramic Fuel Cells, Elsevier, Amsterdam, The Netherlands, 1995.
[2] M. Kuhn, T.W. Napporn, Energies 3 (2010) 57–134.
[3] J.P.P. Huijsmans, F.P.F. van Berkel, G.M. Christie, J. Power Sources 71 (1998) 107–110.
[4] E.V. Tsipis, V.V. Kharton, J. Solid State Electrochem. 15 (2011) 1007–1040.
[5] J.M. Ralph, A.C. Schoeler, M. Krumpelt, J. Mater. Sci. 36 (2001) 1161–1172.
[6] L. Yang, Sh. Wang, K. Blinn, M. Liu, Z. Liu, Z. Chen, M. Liu, Science 326 (2009) 126–129.
[7] J.T.S. Irvine, Perovskite oxide anodes for SOFCs, in: Ishihara (Ed.), Perovskite Oxide for Solid Oxide Fuel Cells, Fuel Cells and Hydrogen Energy, Springer Science and Business Media, LLC, 2009, pp. 167–182.
[8] V.V. Kharton, F.M.B. Marques, A. Atkinson, Solid State Ionics 174 (2004) 135–149.
[9] N. Sammes, Y. Du, in: N. Sammes, A. Smirnova, O. Vasylyev (Eds.), Full Cell Technologies: State and Perspectives, NATO Science Series, Springer, Netherlands, 2005, pp. 19–34.
[10] B.C.H. Steele, in: T. Takahashi (Ed.), High Conductivity Solid Ionic Conductors, World Scientific Press, Singapore, 1989.
[11] J.W. Fergus, J. Power Sources 162 (2006) 30–40.
[12] K. Xie, R. Yan, X. Chen, D. Dong, S. Wang, X. Liu, G. Meng, J. Alloys Compd. 472 (2009) 551–555.

[13] Y. Lin, R. Ran, Y. Guo, W. Zhou, R. Cai, J. Wang, Z. Shao, Int. J. Hydrogen Energy 35 (2010) 2637–2642.
[14] H.J. Park, C. Kwak, K.H. Lee, S.M. Lee, E.S. Lee, J. Eur. Ceram. Soc. 29 (2009) 2429–2437.
[15] K.-D. Kreuer, S.J. Paddison, E. Spohr, M. Schuster, Chem. Rev. 104 (2004) 4637–4678.
[16] T. Hibino, A. Hashimoto, M. Suzuki, M. Sano, J. Electrochem. Soc. 149 (2002) A1503–A1508.
[17] T. Hibino, A. Hashimoto, T. Inoue, J.-I. Tokuno, S.-I. Yoshida, M. Sano, Science 288 (2000) 2031–2033.
[18] A. Demin, P. Tsiakaras, E. Gorbova, S. Hramova, J. Power Sources 131 (2004) 231–236.
[19] A.K. Demin, P.E. Tsiakaras, V.A. Sobyanin, S.Yu. Hramova, Solid State Ionics 152–153 (2002) 555–560.
[20] C.-S. Tu, R.R. Chien, V.H. Schmidt, S.C. Lee, C.-C. Huang, C.-L. Tsai, J. Appl. Phys. 105 (2009) 103504-1–103504-7.
[21] K. Katahira, Y. Kohchi, T. Shimura, H. Iwahara, Solid State Ionics 138 (2000) 91–98.
[22] K.H. Ryu, S.M. Haile, Solid State Ionics 125 (1999) 355–367.
[23] D.A. Medvedev, E.V. Gorbova, A.K. Demin, B.D. Antonov, Russ. J. Electrochem. 47 (2011) 1404–1410.
[24] M. Mogensen, N.M. Sammes, G.A. Tompsett, Solid State Ionics 129 (2000) 63–94.
[25] V.V. Kharton, F.M. Figuiredo, L. Navarro, E.N. Naumovich, A.V. Kovalevsky, A.A. Yaremchenko, A.P. Viskup, A. Carneiro, F.M.B. Marques, J. Frade, J. Mater. Sci. 36 (2001) 1105–1117.
[26] V.A. Sadykov, T.G. Kuznetsova, G.M. Alikina, Y.V. Frolova, A.I. Lukashevich, Y.V. Potapova, V.S. Muzykantov, V.A. Rogov, V.V. Kriventsov, D.I. Kochubei, E.M. Moroz, D.I. Zyuzin, V.I. Zaikovskii, V.N. Kolomiichuk, E.A. Paukshtis, E.B. Burgina, V.V. Zyryanov, N.F. Uvarov, S. Neophytides, E. Kemnitz, Catal. Today 93–95 (2004) 45–53.
[27] C.E. Hatchwell, N.M. Sammes, G.A. Tompsett, I.W.M. Brown, J. Eur. Ceram. Soc. 19 (1999) 1697–1703.
[28] A. Atkinson, Solid State Ionics 95 (1997) 249–258.
[29] T. Inoue, T. Setoguchi, K. Eguchi, H. Arai, Solid State Ionics 35 (1989) 285–291.
[30] S. Cho, Y.-N. Kim, J.-H. Kim, A. Manthiram, H. Wang, Electrochim. Acta 56 (2011) 5472–5477.
[31] D. Hirabayashi, A. Tomita, T. Hibino, M. Nagao, M. Sano, Electrochem. Solid State Lett. 10 (2004) A318–A320.
[32] A. Tomita, Y. Tachi, T. Hibino, Electrochem. Solid State Lett. 11 (2008) B68–B70.
[33] T. Mori, H. Yamamura, J. Mater. Synth. Process. 6 (1998) 175–179.
[34] D.L. Maricle, T.E. Swarr, S. Karavolis, Solid State Ionics 52 (1992) 173–182.
[35] E.Yu. Pikalova, V.G. Bamburov, A.A. Murashkina, A.D. Neuimin, A.K. Demin, S.V. Plaksin, Rus. J. Electrochem. 47 (2011) 690–696.
[36] S. Yamaguchi, N. Yamada, Solid State Ionics 162–162 (2003) 23–29.
[37] J.-X. Wang, L.-P. Li, B.J. Campbell, Z. Lv, Y. Ji, Y.F. Xue, W.-H. Su, Mater. Chem. Phys. 86 (2004) 150–155.
[38] T. Ohzeki, S. Hasegawa, M. Shimizu, T. Hashimoto, Solid State Ionics 180 (2009) 1034–1039.
[39] E. Yu. Pikalova, A.A. Murashkina, V.I. Maragou, A.K. Demin, V.N. Strekalovsky, P.E. Tsiakaras, Int. J. Hydrogen Energy 36 (2011) 6175–6183.
[40] A. Venkatasubramanian, P. Gopalan, T.R.S. Prasanna, Int. J. Hydrogen Energy 35 (2010) 4597–4605.
[41] W. Sun, Y. Jiang, Y. Wang, S. Fang, Z. Zhu, W. Liu, J. Power Sources 196 (2011) 62–68.
[42] M. Khandelwal, A. Venkatasubramanian, T.R.S. Prasanna, P. Gopalan, J. Eur. Ceram. Soc. 31 (2011) 559–568.
[43] S. Elangovan, B.G. Nair, T. Small, et al., Patent 8,012,380 B2 (USA) 2011.
[44] B. Zhu, X. Liu, T. Schober, Electrochem. Commun. 6 (2004) 378–383.
[45] Z. Shao, W. Zhou, Z. Zhu, Prog. Mater. Sci. 57 (2012) 804–874.
[46] F. Deganello, G. Marchì, G. Deganello, J. Eur. Ceram. Soc. 29 (2009) 439–450.
[47] B.Y. Ma, X. Wang, S. Li, M.S. Toprak, B. Zhu, M. Muhammed, Adv. Mater. 22 (2010) 1640–1644.
[48] K.C. Patil, M.C. Hegde, T. Rattan, S.T. Aruna, Chemistry of Nanocrystalline Oxide Materials. Combustion Synthesis, Properties and Applications, World Scientific Publishing Company, Singapore, 2008.
[49] D. Lin, Q. Wang, K. Peng, L.L. Shaw, J. Power Sources 205 (2012) 100–107.
[50] W. Chen, F. Li, J. Yu, Mater. Lett. 60 (2006) 57–60.
[51] http://www.iep.uran.ru/razzr/nanoim/razr_14.html.
[52] R.R. Chien, C.-S. Tu, V.H. Schmidt, S.-C. Lee, C.-C. Huang, Solid State Ionics 181 (2010) 1251–1257.
[53] M.G. Zimicz, I.O. Fábregas, D.G. Lamas, S.A. Larrondo, Mater. Res. Bull. 46 (2011) 850–857.
[54] W. Chen, F. Li, J. Yu, Y. Li, J. Rare Earths 24 (2006) 434–439.
[55] H. Palneedi, V. Mangam, S. Das, K. Das, J. Alloys Compd. 509 (2011) 9912–9918.
[56] N. Zakowsky, S. Willimson, J.T.S. Irvine, Solid State Ionics 176 (2005) 3019–3026.
[57] R. Köferstein, D. Hesse, S.G. Ebbinghaus, Solid State Ionics 203 (2011) 52–56.
[58] J. Bera, D. Sarkar, J. Electroceram. 11 (2003) 131–137.
[59] F.L. Chen, O.T. Sørensen, G.Y. Meng, D.K. Peng, J. Therm. Anal. Calor. 49 (1997) 1255–1261.
[60] M.R. Kosinski, R.T. Baker, J. Power Sources 196 (2011) 2498–2512.
[61] X. Wu, H. Wang, R. Peng, G. Meng, Solid State Ionics 192 (2011) 611–614.
[62] C. Zhang, H. Zhao, S. Zhai, Int. J. Hydrogen Energy 36 (2011) 3649–3657.
[63] L. Li, J.C. Nino, J. Eur. Ceram. Soc. 32 (2012) 3543–3550.
[64] M. Amsif, D. Marrero-Lopez, J.C. Ruiz-Morales, S.N. Savvin, M. Gabás, P. Nunez, J. Power Sources 196 (2011) 3461–3469.
[65] R. Köferstein, R. Jäger, S.G. Ebbinghaus, J. Mater. Sci. 45 (2010) 6521–6527.
[66] K.S. Knight, Solid State Ionics 145 (2001) 275–294.
[67] E.Yu. Pikalova, V.I. Maragou, A.N. Demina, A.K. Demin, P.E. Tsiakaras, J. Power Sources 181 (2008) 199–206.
[68] Y. Zheng, S. He, L. Ge, M. Zhou, H. Chen, L. Guo, Int. J. Hydrogen Energy 36 (2011) 5128–5135.
[69] S. Huang, Q. Lu, S. Feng, G. Li, C. Wang, J. Power Sources 199 (2012) 150–154.
[70] E. Gorbova, V. Maragou, D. Medvedev, A. Demin, P. Tsiakaras, J. Power Sources 181 (2008) 207–213.
[71] K. Xie, R. Yan, X. Xu, X. Liu, G. Meng, J. Power Sources 187 (2009) 403–406.
[72] X. Zhou, L. Liu, J. Zhen, S. Zhu, B. Li, K. Sun, P. Wang, J. Power Sources 196 (2011) 5000–5006.
[73] G.B. Balazs, R.S. Glass, Solid State Ionics 76 (1995) 155–162.
[74] R. Peng, C. Xia, D. Peng, G. Meng, Mater. Lett. 58 (2004) 604–608.
[75] R. Peng, C. Xia, Q. Fu, G. Meng, D. Peng, Mater. Lett. 56 (2002) 1043–1047.
[76] P. Ranran, W. Yan, Y. Lizhai, M. Zongqiang, Solid State Ionics 177 (2006) 389–393.
[77] K.D. Kreuer, Annu. Rev. Mater. Res. 33 (2003) 333–359.
[78] E. Fabbri, L. Bi, D. Pergolesi, E. Traversa, Adv. Mater. 24 (2012) 195–208.
[79] Y.-P. Fu, S.-H. Chen, J.-J. Huang, Int. J. Hydrogen Energy 35 (2010) 745–752.
[80] Y. Zheng, M. Zhou, L. Ge, S. Li, H. Chen, L. Guo, J. Alloys Compd 509 (2011) 1244–1248.
[81] J.-S. Park, J.-H. Lee, H.-W. Lee, B.-K. Kim, Solid State Ionics 192 (2011) 88–92.
[82] M. Oishi, S. Akoshima, K. Yashiro, K. Sato, J. Mizusaki, T. Kawada, Solid State Ionics 179 (2008) 2240–2247.
[83] M. Oishi, S. Akoshima, K. Yashiro, K. Sato, J. Mizusaki, T. Kawada, Solid State Ionics 180 (2008) 127–131.
[84] W. Sun, W. Liu, J. Power Sources 217 (2012) 114–119.
[85] Q. Jiang, J. Cheng, R. Wang, Y. Fan, J. Gao, J. Power Sources 206 (2012) 47–52.